Biological flow networks: Antagonism between hydrodynamic and metabolic stimuli as driver of topological transitions

Felix Kramer [1,2,*] and Carl D. Modes [1,2,3,†]

[1]*Max Planck Institute for Molecular Cell Biology and Genetics (MPI-CBG), Dresden 01307, Germany*
[2]*Center for Systems Biology Dresden (CSBD), Dresden 01307, Germany*
[3]*Cluster of Excellence, Physics of Life, TU Dresden, Dresden 01307, Germany*

(Received 18 January 2022; accepted 15 December 2022; published 17 May 2023)

A plethora of computational models have been developed in recent decades to account for the morphogenesis of complex biological fluid networks, such as capillary beds. Contemporary adaptation models are based on optimization schemes where networks react and adapt vessel conductance toward given flow patterns. Recent numeric studies on network morphogenesis, incorporating uptake of metabolites by the embedding tissue, have indicated this conventional approach to be insufficient. Here, we systematically study a hybrid model intended to generate space-filling perfusion as well as optimal filtration of metabolites. As a result, we find hydrodynamic stimuli (wall-shear stress) and filtration based stimuli (uptake of metabolites) to be antagonistic as hydrodynamically optimized systems have suboptimal uptake qualities and vice versa. We show that a switch between optimization regimes is typically accompanied with a transition between topologically redundant meshes and spanning trees. Depending on the metabolite demand and uptake capabilities of the adapting networks, we further demonstrate the existence of nullity reentrance as a function of dissipation and the development of compromised phenotypes such as dangling nonperfused vessels and bottlenecks.

DOI: 10.1103/PhysRevResearch.5.023106

I. INTRODUCTION

Physiological organization, like gravitation, is a "stubborn fact" and it is one task of theoretical physiology to find quantitative laws, which describe organization in its various aspects.–C. D. Murray, in [1].

The physiological organization referred to here by C. D. Murray nearly a hundred years ago is the morphogenesis of vascular networks. And true to his statement, Murray derived a theoretical framework based on simple hydrodynamic assumptions, which would account for branching patterns emerging in the arteriole regime, now known as *Murray's law*. By minimizing the overall shear stress for a volume constrained lumen of a model network, he would determine the flow of scientific inquiry in this field for the rest of the century. And yet, recent studies on metabolite transport in flow networks [2–4] have demonstrated, along with similar studies on flow homogeneity [5], that purely shear stress based morphogenesis models of the capillary bed may be in dire need of revision.

Biological flow networks do not grow fully developed and matured in their final and functional form, but seem to self-organize bit by bit in the context of their surrounding tissue, perfusion and other stimuli over a long time span (compared to hydrodynamic time scales) [6,7]. Most interestingly, it has been repeatedly shown that this development is mechanotransductional in nature, coupling complex biochemical signaling to mechanical cues such as wall-shear stress [8–11]. This has been demonstrated to be the case in a variety of vertebrate model organisms [10,12,13], for endothelium and epithelium alike. Stress based adaptation seems universally present in the biosphere, as it has further been observed in plants [14] and slime mold [15]. A recurring problem in these studies however is to identify stimuli causing the complex topology of capillary networks, i.e., resilient, space-filling meshes containing hydrodynamically favorable "highways", defying Murray's law [16–18]. Subsequently, more complex stimuli such as growth, noisy flow patterns, and hemodynamical complications have been rigorously discussed in computational studies, and have been found to account for complex topological changes in the respective networks [19–24].

Although these abstract schemes have been very successful in accounting for the topological complexity of biological flow networks, most disregard the physiological aspect entirely: It is general consensus that any major exchange of metabolites between vasculature and tissue, such as oxygen, salts, glucose, proteins etc., is performed on the capillary level and poses a valid stimuli for morphogenesis [25,26]. Subsequently, identifying remodeling mechanisms and efficient network architectures has become crucial to address vasculature pathology, e.g., tumor angiogenesis [27–29], or the intelligent design of synthetic supply systems [30,31]. Yet, to our knowledge, only a handful of suggestions have

*felixuwekramer@proton.me
†modes@mpi-cbg.de

been made for heuristic stimuli models ensuring perfusion of vascular networks with metabolites [32,33]. These initial approaches have been lacking a thorough discussion of the actual uptake capabilities of the embedding tissue as well as an incorporation into the current discussion of flow network optimality. Recently two frameworks have been re-visited to advance this inquiry: the Taylor dispersion model [34] and the Krogh model [35]. Taylor dispersion models consider metabolite transport to be a nontrivial interplay between the flow pattern and diffusion while incorporating a concentration dependent solute uptake along the vessel surfaces. This dispersion model was initiated as an appropriate metabolite transport model during slime mold morphogenesis [36,37], but has since been utilized to account for the adaptation phenomena found in plants and vertebrate capillaries [2,3]. On the other hand, Garvrilchenko *et al.* [4] suggested an adaptation model on the grounds of the Krogh model to account for the explicit supply of discrete service elements in the tissue. This transport model also incorporates the convection of solute along idealized vessels in combination with metabolite diffusion from the channel surface into the surrounding tissue environment.

Inspired by these studies we propose a minimal hybrid model that takes into account stimuli in the form of the actual metabolite uptake of the surrounding tissue together with the conventional wall-shear stress approach, and incorporate these into the cost function scheme. We begin in Sec. II by giving a brief illustration of the model framework, including the Kirchhoff network approach and introduction of cost functions for capillary flow networks. Next we present the numeric results, displaying the antagonistic interplay of uptake and shear stress driven morphogenesis as well as the topological ramifications and frustrated network formations, such as dangling branches and bottlenecks, see Sec. III. We conclude and discuss these results in Sec. IV, pointing out the limitations of our model and parameter space search as well as the emerging phenomena of redundancy re-entrant behavior and plexus dependencies.

II. METABOLITE TRANSPORT AND NETWORK ADAPTATION

In this section we give a brief overview on the theoretical framework of fluid advection and metabolite transport Kirchhoff networks. Readers already familiar with these concepts may skip forward to Sec. III.

A. Approximating capillary beds as Kirchhoff networks

We model capillary networks of interest as a composition of thin fluid conducting channels, abstracted as a graph of E edges and N vertices. These vertices will represent branching points of the real biological system and are assumed to hold no fluid volume on their own. Each edge e carries a current f_e such that at any vertex the sum of all currents is equal to a nodal source s_n. Further, every edge is characterized by a conductivity K_e relating the flow to the potential difference Δp_e according to Ohm's Law. One may write these relations using the graph's incidence matrix $\boldsymbol{B}$ as

$$s_n = \sum_e B_{ne} f_e, \tag{1}$$

$$f_e = K_e \Delta p_e, \tag{2}$$

where (1) is also referred to as a "Neumann boundary condition", fixing the peripheral currents [38]. The resulting equation system determines the networks flow and pressure landscape, for further details see [39,40]. Here, we consider a system of Hagen–Poiseuille flows, which allows one to express the current as the volume flow rate $f = \frac{\pi R^4}{8\eta L}\Delta p$ [41]. This ansatz considers the approximation of thin cylindrical vessels of radius R and length L being perfused laminarly by a fluid of viscosity η. Such a vessel system can be directly described via the presented Kirchhoff network by setting the conductivity on each link to be $K_e = \frac{\pi R_e^4}{8\eta L_e}$. Here, we do not incorporate any non-Newtonian fluid properties though they may arise, for example, in blood.

B. Metabolite transport in lumped network models

Next, we incorporate the metabolite transport of a single species of molecules across the network. To do so, we take an approach inspired by Heaton *et al.* [42].

Solute is transported by means of diffusion and advection along a quasi-one-dimensional vessel, neglecting lateral perturbations or any dependencies of the flow velocity on the concentration levels. While molecules are drifting down the channel they are absorbed at constant rate by the channel walls, which form the periphery to the embedding tissue, see Fig. 1. Subsequently, we formulate the dynamics of the concentration $\bar{c}(z,t)$ along any channel's symmetry axis (z axis) by using the continuity equation,

$$\partial_t \bar{c} = D\partial_{zz}\bar{c} - \bar{u}\partial_z \bar{c} - \beta \bar{c}. \tag{3}$$

Here, the diffusion constant is D, the advection velocity is $\bar{u}$ and the surface absorption rate is β. We use the notation $\bar{(\cdot)}$ to identify cross section averages, which denote the relevant factors in our deduction. Although we will soon discuss the dynamics of an adapting network, we would like to point out here that the hydrodynamic time scales are considerably shorter than the time-scales of adaptation. Therefore, we consider the system to reach a stationary regime between adaptation steps and calculate solutions only for $\partial_t \bar{c} = 0$. The resulting ordinary differential equation may readily be solved (using the notation $z^* = z/L$),

$$0 = \frac{D}{L^2}\partial_{zz^*}\bar{c} - \frac{\bar{u}}{L}\partial_{z^*}\bar{c} - \beta\bar{c} \tag{4}$$

$$\Rightarrow \bar{c}(z^*) = X_0 e^{\lambda_0 z^*} + X_1 e^{\lambda_1 z^*} \tag{5}$$

$$\text{with } \lambda_{0/1} = \frac{\bar{u}L}{2D} \pm \frac{\sqrt{\left(\frac{\bar{u}L}{D}\right)^2 + \frac{4\beta L^2}{D}}}{2} \tag{6}$$

$$= \frac{1}{2}(Pe \pm \sqrt{Pe^2 + \beta^*}). \tag{7}$$

One may deduce from the channel's boundaries $\bar{c}(z=0) = \bar{c}_0$, $\bar{c}(z=L) = \bar{c}_L$ that $X_0 = \frac{\bar{c}_L - \bar{c}_0 e^{\lambda_1}}{e^{\lambda_0} - e^{\lambda_1}}$ and $X_1 = \frac{\bar{c}_0 e^{\lambda_0} - \bar{c}_L}{e^{\lambda_0} - e^{\lambda_1}}$. Here

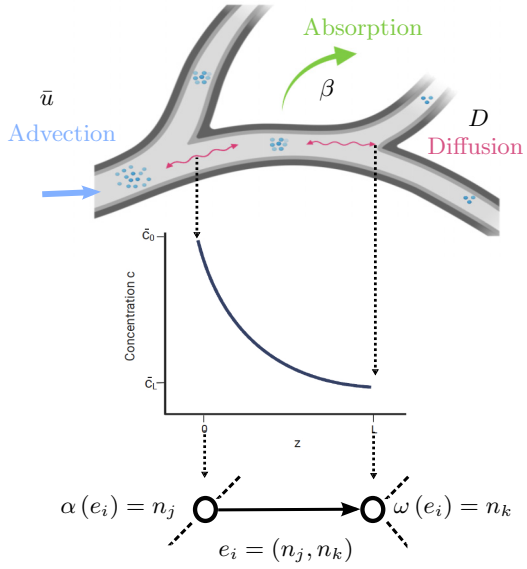

FIG. 1. Toy model for metabolite transport [43]. *(Top)* A species of metabolites is transported via convection (advection-diffusion) along the (quasi-) one-dimensional vessel segments while being absorbed on by the vessels' surfaces. *(Middle)* Seeing the vessel system as a compound of single channels, one may compute the stationary concentration profile given the boundary concentrations c_0, c_L at the vessel's endings. *(Bottom)* The vessel network will be abstracted as a (arbitrarily) directed graph, with branching points as vertices n and vessel segments in between as edges e. Subsequently each edge has individual boundary concentrations $c_{\alpha(e)}$, $c_{\omega(e)}$.

we define the Peclet number Pe and the dimensionless absorption rate β^* as

$$\mathrm{Pe} = \frac{\bar{u}L}{D}, \tag{8}$$

$$\beta^* = \frac{4\beta L^2}{D}. \tag{9}$$

Now we solve these equations for arbitrarily directed edges e, whose starting and end points we label as $\alpha(e)$, $\omega(e)$. As every edge e is a channel with concentrations $c_e(z)$, we use a nodal notation as $\bar{c}_e(0) = \bar{c}_{\alpha(e)}$, $\bar{c}_e(L) = \bar{c}_{\omega(e)}$. Each link is further assigned its cross section area as $A_e = \pi R_e^2$, and we introduce the abbreviation $x_e = \sqrt{\mathrm{Pe}_e^2 + \beta^*}$. Using this notation we may rewrite the profiles $\bar{c}_e(z)$ along each link e,

$$\bar{c}_e(z^*) = \frac{\mathrm{e}^{\frac{\mathrm{Pe}_e z^*}{2}}}{\sinh\left(\frac{x_e}{2}\right)}\left\{\bar{c}_{\omega(e)}\sinh\left(\frac{x_e z^*}{2}\right)\mathrm{e}^{-\frac{\mathrm{Pe}_e}{2}} - \bar{c}_{\alpha(e)}\sinh\left(\frac{x_e[z^*-1]}{2}\right)\right\}. \tag{10}$$

Therefore we may calculate the solute flux on each link as

$$I_e(z) = A_e[\bar{u}_e\bar{c}_e(z) - D\partial_z\bar{c}_e(z)] \tag{11}$$

$$= q_e[\mathrm{Pe}_e\bar{c}_e(z^*) - \partial_{z^*}\bar{c}_e(z^*)]. \tag{12}$$

To increase readability we introduce the dimensionless flux parameter $q_e = \frac{A_e D}{L}$ and use the notation $I_e(0) = I_{\alpha(e)}$, $I_e(L) = I_{\omega(e)}$. Then we formulate the boundary conditions for the flux analog to the Kirchhoff conditions of flow (1). In particular we have a balance of solute in- and outflux J at each vertex,

$$J_n = \sum_{e\in out(n)} I_{\alpha(e)} - \sum_{e\in in(n)} I_{\omega(e)}, \tag{13}$$

where $out(n)$, $in(n)$ indicate the index sets of directed edges pointing outwards or inwards of a vertex n. We solve these equations in accordance to the method described in [44], see Appendix A for more detail. Sorting the equations (12) and (13) for the concentration terms one can rewrite the entire equation system as

$$\boldsymbol{M}\cdot\boldsymbol{c} = \boldsymbol{J} \tag{14}$$

with an asymmetric matrix $\boldsymbol{M}$ whose entries are dependent only on Pe and β^*. Having done so we are effectively computing the stationary solution of e equations of the form (3) with n boundaries, which are for us to define [see Kirchhoff problem (1)]. As in previous studies we choose a system with absorbing boundaries, setting a subset of nodes $\boldsymbol{c}_0 = \boldsymbol{0}$ at the network's sinks, while setting $J_n > 0$ for any node with $s_n > 0$ and $J_n = 0$ otherwise. One may calculate the nodal concentrations $\bar{c}_n$, as well as the total solute uptake per edge e, as $\Phi_e = \beta L\int_0^1 \bar{c}_e(z^*)dz^*$ and get

$$\Phi_e = q_e\left\{\bar{c}_{\alpha(e)}\left[x_e\coth\left(\frac{x_e}{2}\right) - \frac{x_e\mathrm{e}^{\frac{\mathrm{Pe}_e}{2}}}{\sinh\left(\frac{x_e}{2}\right)} + \mathrm{Pe}_e\right] + \bar{c}_{\omega(e)}\left[x_e\coth\left(\frac{x_e}{2}\right) - \frac{x_e\mathrm{e}^{-\frac{\mathrm{Pe}_e}{2}}}{\sinh\left(\frac{x_e}{2}\right)} - \mathrm{Pe}_e\right]\right\}. \tag{15}$$

Note that the effective uptake Φ_e of a vessel is entirely determined by the landscape of Peclet numbers Pe and local uptake rates β. We shall capitalize on this phenomenon in the next sections to construct an adaption scheme, which enables a regulation of effective metabolite uptake on the grounds of flow.

C. Multi-target driven radius optimization

In order to model the dynamic adaptation of rudimentary flow networks we follow the ansatz of characterizing such a transport system with a cost function Γ. Any minimization of Γ may be performed via the radial (and topological) adaptations of the flow network, and therefore determine its long-term pruning behavior. Hence one may formulate a generic cost for vessel systems as proposed before by Bohn *et al.* [45],

$$\Gamma = \sum_e\left(\frac{f_e^2}{K_e} + \alpha_0 K_e^{1/2}\right), \tag{16}$$

where the first term $(\frac{f_e^2}{K_e})$ is the power dissipation of the flow and the second is a conductance cost $(\alpha_0 L_e K_e^{1/2})$, with proportionality factor α_0. Minimizing the first term encapsulates the notion of reducing the overall wall shear stress imposed on the tubal cells [46]. The second term formulates a constraint on the conductance the biological organism may deploy or sustain. In particular, for Hagen-Poiseuille flows this can be seen as a radial constraint, preventing arbitrarily large vessel volumes. These functions may be tailored for a variety of biological flow networks [5].

In this study we consider a dissipation-volume minimizing system in combination with the metabolic needs of the surrounding tissue. To reduce the problem's complexity we will consider the special case of constant channel lengths throughout the system $L_e = L$. Similar to previous setups studied in Refs. [3,32,35] we will focus here on a vessel network embedded in a tissue environment, where each vessel is surrounded by the service volume it supplies. Generally speaking these service volumes are ensembles of cells forming a bulk environment, signaling affiliated vessels to adjust supply properly, e.g., by downstream signaling (via convection) or up-stream signaling (via conduction) [7]. Here, individual vessels are supposed to act as *fair players* by adapting toward a specific metabolite need. This may correspond to cases were tissues are able to prevent over-saturation, e.g., actively avoid toxic overdosing.

We consider each vessel to be surrounded by tissue to which it supplies a metabolite, as described in Sec. II B. Further, every such element of tissue i demands a basic influx of solute $\Phi_{0,i}$ possibly mismatching the current uptake Φ_e provided by the embedded vessels. We expand the cost (16) by defining a mismatch cost $S(\mathbf{\Phi}, \mathbf{\Phi}_0) \geqslant 0$ and write

$$\Gamma = S(\mathbf{\Phi}, \mathbf{\Phi}_0) + \sum_e \left(\alpha_1 \frac{f_e^2}{K_e} + \alpha_0 K_e^{1/2} \right). \tag{17}$$

We construct $S(\mathbf{\Phi}, \mathbf{\Phi}_0)$ in such a way that deviation from the demand $\mathbf{\Phi}_0$ is penalized. We minimize the cost (17) using a gradient descent approach where vessels are allowed to adjust their individual radii. Subsequently one will have the channel conductivities and local Peclet numbers changed. The impact of the simultaneously given dissipation-volume constraints, as in (16), is tuned via the coupling parameters α_0, α_1. Increased volume penalties α_0 naturally lead to smaller vessel structures, simultaneously increasing Pe and therefore hindering solute uptake. On the other hand, increasing the dissipation factor α_1 will generally increase vessel size for perfused vessels and decrease local Pe, thereby increasing uptake.

D. Measuring topological network redundancy and metabolite filtration

In order to quantify the topological changes occurring in an adapting system, we monitor the amount of cycles in a network [47],

$$Z = E - (N - 1). \tag{18}$$

We use this metric in the following way: The network is first initialized for a densely reticulated system, a so-called plexus. Links are no longer updated when their radius falls below a critical threshold r_c. We call such edges *pruned*, which corresponds to the biological phenomenon of having a vessel degenerate and collapse. At the end of each optimization we remove all pruned edges and disconnected vertices from the graph and recalculate the remaining number of cycles. We then define the relative nullity of an equilibrated network,

$$\varrho = \frac{E - N + 1}{Z_0} \tag{19}$$

as an order parameter, where Z_0 is the initial number of cycles before adaptation. Hence $\varrho = 0$ corresponds to a treelike network while $\varrho > 0$ captures the relative amount of redundancy in comparison to the initial plexus. Further we monitor the relative solute uptake rate, or rather filtration rate, of the network as

$$\sigma = \log_{10} \left[\frac{\sum_e \Phi_e}{\sum_{n, J_n \geqslant 0} J_n} \right]. \tag{20}$$

Hence we get $\sigma \to 0$ if the network's vessel surface absorbs the entire injected solute and $\sigma \to -\infty$ if there is no absorption whatsoever. Generally we intend to construct the mismatch $S(\mathbf{\Phi}, \mathbf{\Phi}_0)$ such that a certain value of σ is reached, reflecting the notion that the supplied tissue needs to meet a certain total solute demand.

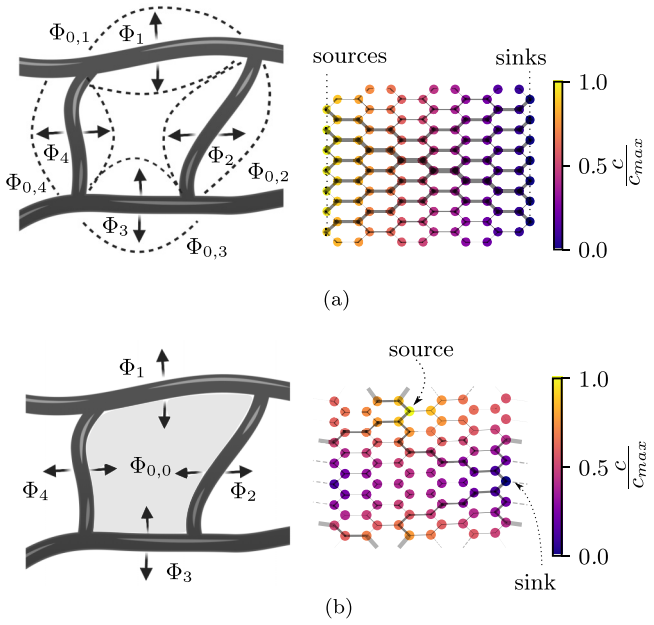

FIG. 2. Uptake models [43] and network plexi (with edge thickness representing radii and nodal concentrations color-coded): (a) Link-wise demand model, with edge-wise demand $\Phi_{0,e}$ and responding supplies Φ_e. The planar plexus is initialized with multiple sources and absorbing boundaries on opposing graph sides. (b) Volume-demand model, with enclosed tiles having a demand $\Phi_{0,v}$ responded to by affiliated edges with supply Φ_e. The plexus is initialized with periodic boundaries and a dipole source-sink configuration. Transparent, marked links indicate periodic boundaries.

III. SIMULATING DEMAND-SUPPLY ADAPTATION IN CAPILLARY BEDS

In this section we present the simulation setup and numeric results as well as the implications of the hybrid model framework presented in the previous sections. In particular we will interrogate Eq. (17) for two uptake scenarios: Link-wise demand-supply and volume-wise demand-supply, see Fig. 2. For each case we define individual mismatch functions $S(\mathbf{\Phi}, \mathbf{\Phi}_0)$. We minimize the metabolic cost (17) using a gradient descent approach identifying local minima for random plexus initializations. In Appendix B we give a detailed account of the derivation of the respective dynamical systems for Γ, which define the equations of motion $\partial_t r_e$ for the vessel

radii. These equation systems are solved until a stationary state is reached and subsequent evaluation, according to the measures in Sec. II D, is performed.

A. Linkwise demand-supply model

We first consider a vessel system as shown in Fig. 2(a), where each vessel supplies exactly one service volume. Each such service volume demands an optimal influx of solute $\Phi_{0,e}$ possibly mismatching the current uptake Φ_e provided by the embedded vessel. The metabolite transport is computed as discussed in Sec. II B. We formulate the uptake mismatch as a cost that reads

$$S(\mathbf{\Phi}, \mathbf{\Phi}_0) = \sum_e (\Phi_e - \Phi_{0,e})^2. \tag{21}$$

Hence we write for the system's total cost (17),

$$\Gamma = \sum_e \left[(\Phi_e - \Phi_{0,e})^2 + \alpha_1 \frac{f_e^2}{K_e} + \alpha_0 K_e^{\frac{1}{2}} \right]. \tag{22}$$

In fact if the service volume demands are identical for the entire network we recreate the optimization framework studied in [3] extended by wall-shear stress driven pruning. We impose sources $s_n > 0$ and solute influx $J_n > 0$ on all vertices of one side of the graph and sinks and absorbing boundaries on the opposing side. We refer to these vertices also as terminal or peripheral nodes. Internal vertices are set source- and influx-free, i.e., $s_n = 0, J_n = 0$. In this study we are concerned with four essential model parameters: absorption rate β^*, demand Φ_0, dissipation feedback α_1, and volume penalty α_0. We initialize the system for selected absorption rates β^* and demand Φ_0 combinations, while scanning systematically for wide ranges of the dissipation feedback α_1 and the volume penalty α_0. We set all vessels to correspond to a demand $\Phi_{0,e}$ such that the network's demanded filtration rate corresponds to

$$\sigma_0 = \log_{10}\left[\frac{\sum_e \Phi_{0,e}}{\sum_{v,J_v>0} J_v} \right]. \tag{23}$$

For the presented simulations, we initialize $\Phi_{0,e}$ homogeneously across the network, as well as β^*. From here on we will discuss the demand in terms of the total network's demand σ_0. Following the adaptation algorithm, as described in the previous section, we find the system's stationary states and analyze those for their nullity ϱ and actual filtration rate σ. The columns in Fig. 3 display these metrics, while Fig. 4 depicts stationary network formations for three significant (σ_0, β^*) variations.

The first case, $\sigma_0 = 0$ and $\beta^* = 10^{-3}$, depicted in Figs. 3(a) and 4(a), represents the unfavorable case of high demand paired with low absorption capability, prone to undersupply. As depicted in Fig. 4(a) we can show that increasing α_1 will generally result in a nullity transition, displaying frustrations for the reticulated case as well as the formation of dangling branches not connected to any sinks. Nevertheless, we find the reticulated states in good agreement with a network-wide adjustment toward the demand σ_0.

For small α_1, we observe that the majority of vessels in the network are dilated while most peripheral connections

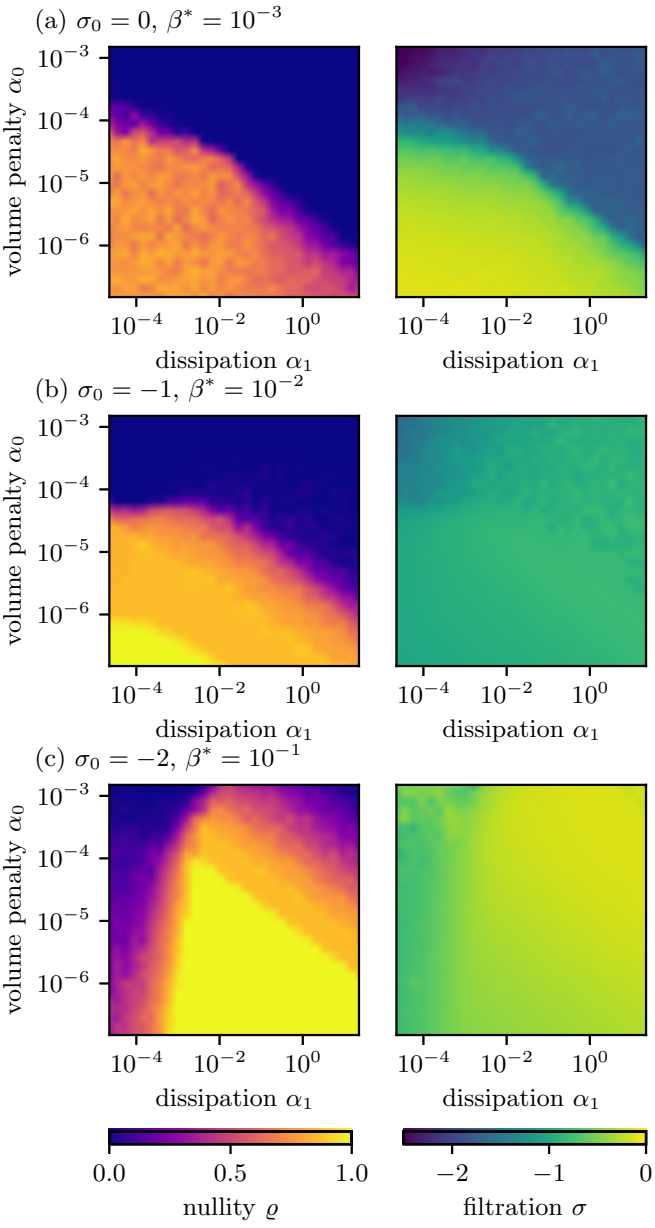

FIG. 3. Stationary states for the link-wise demand-supply problem (22): Color-coded state diagrams indicate the network nullity ϱ (left column) and accumulated filtration σ (right column) for selected (σ_0, β^*).

to the sinks are degenerated and seemingly near to collapse, see Appendix C. Hence by dilating the bulk of vessels one minimizes the Peclet numbers Pe in the system(boundary conditions dictate a constant volume throughput), which maximizes individual vessel uptake. In order to guarantee high filtration, as many vessels as possible have to stay open, naturally resulting in a reticulated network state. Note, that no significant concentration gradient is present in the bulk, see Appendix C.

At the periphery, incident to outlet nodes, decreasing the size of vessels leads to a sudden increase of the Peclet number Pe and allows for rapid solute clearance in accordance with the boundary conditions. These small vessels experience dra-

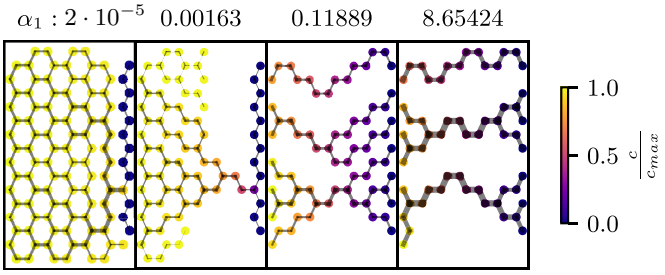

(a) $\sigma_0 = 0$, $\beta^* = 10^{-3}$, $\alpha_0 = 4.5 \cdot 10^{-5}$

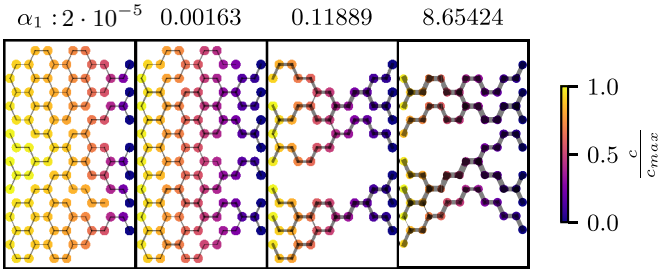

(b) $\sigma_0 = -1$, $\beta^* = 10^{-2}$, $\alpha_0 = 4.5 \cdot 10^{-5}$

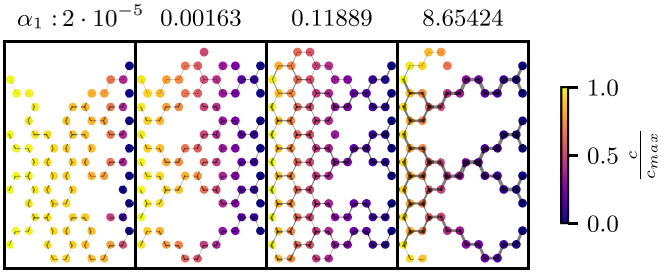

(c) $\sigma_0 = -2$, $\beta^* = 10^{-1}$, $\alpha_0 = 8 \cdot 10^{-4}$

FIG. 4. Stationary network formations for the linkwise demand-supply problem. Depicted are formations for selected demands σ_0, absorption rates β^*, volume penalties α_0, and dissipation feedbacks α_1 after minimizing (22). All systems were initialized with peripheral sink-source vertices. The nodal concentrations are color coded and link thickness is indicating edge radii.

matically higher wall-shear stress than the rest of the system, but due to small α_1 no significant growth feedback is posed. Subsequently, increasing α_1 breaks this patterning, as it will open up exactly these high-shear stress vessels, which subsequently decreases Pe at the periphery. This in turn changes the concentration landscape into a network-wide gradient. We further observe the break down of weakly perfused vessels, which are not anymore stabilized by the uptake mechanism.

The second case, $\sigma_0 = -1$ and $\beta^* = 10^{-2}$, depicted in Figs. 3(b) and 4(b), features reduced demand paired with increased absorption capability. Here we see once again a nullity breakdown due to increase of α_0 and α_1, yet the corresponding filtration diagrams and concentration profiles are considerably different. As shown in Fig. 4(b), even for marginal α_1 a system spanning concentration gradient is readily abundant, see also Appendix C, and no degeneration of peripheral vessels takes place, as previously observed. The filtration diagrams in Fig. 4(b) illustrate that a seeming match of metabolite uptake is achieved in good approximation, yet deviates for large volume penalties α_0. Further, we see that dissipation feedback dominated regimes, where spanning trees emerge as the distinct graph topology, still reasonably well fulfill the initial filtration demand. One should keep in mind that a match in overall filtration σ does not necessarily imply an actual match of all absorbing vessels, nor does it ensure laterally extended supply.

The third case, $\sigma_0 = -2$ and $\beta^* = 10^{-1}$, depicted in Figs. 3(c) and 4(c), poses another unfavorable scenario where low demand is paired with high absorption rates, prone to oversupply. Naturally we should observe general vessel degeneration in order to increase Pe, which in turn diminishes solute uptake. Subsequently we would operate in a system that minimizes the number of vessels and experiences high wall-shear stress for the remaining vessels in the network. That is indeed the case and may be observed for the network plots in Fig. 4(c) at low α_1. Nevertheless we observe the emergence of reentrant behavior in the nullity diagram in case of increasing dissipation feedback α_1. The sharpness of this transition is sensitive to the choice of r_c. To our knowledge such reentrance has not been previously encountered in other network morphogenesis models. As the phenomenon of reentrant phase behavior can be caused by underlying antagonistic interactions, we hypothesize the transition to occur in the following way: Approaching the nullity transition from the left-hand flank for small α_1, we find the system "loaded" with high wall-shear stresses as high Peclet numbers are abundant with a minimal set of channels, which are not allowed to grow and redistribute load due to the small dissipation feedback. Increasing α_1 further, one is able to stabilize previously collapsing vessels and the system encounters a nullity transition. This process is still overshadowed by the fact that Peclet numbers have to be kept high by reducing overall vessel sizes. Increasing α_1 pushes the system once again to the wall-shear stress dominated regime. Subsequently we observe the emergence of large conducting channels and a topological transition back towards spanning trees. Although we find poor adjustment of the system toward low filtration rates we observe this relaxation to push the filtration rate up, as Peclet numbers decrease, see Fig. 3(c).

B. Volume-element demand-supply model

So far we have shown that demand-supply models are capable of rich phase behavior due to the antagonistic interaction of hydrodynamic and metabolic adaptation. Yet the current approach dictates only one supplying vessel for any service element, meaning that pruned vessels result in entirely non-supplied regions. Thus, in a real system no plexus could ever be pruned without killing multiple service elements. In this section, we alter the previous setup and focus our studies on a system defined by shared volume elements rather than single vessel service volumes. Here, each service volume element v is in contact with a set of vessels supplying individually a fraction of their uptake Φ_e, see Fig. 2(b). Each volume v demands an influx of solute $\Phi_{0,v}$ potentially mismatching the

summed uptake $\sum_{e\in E_v}\Phi_e$, provided by the attached vessel set E_v. We do so following a similar model by Gavrilchenko *et al.* [4], which allows us to introduce redundancy and cooperative metabolite supply in the overall demand-supply scheme. Similar to the previous section's setup, we propose a cost for volume-service of the form

$$S(\mathbf{\Phi},\mathbf{\Phi}_0)=\sum_v\left\{\Phi_{0,v}-\sum_{e\in V}w_e\Phi_e\right\}^2. \tag{24}$$

Here we denote supply weights w_e, which encapsulate the effective share that a supplying vessel provides, enabling further tuning of essential and redundant vessels in the adjustment process. Hence we formulate the system's overall metabolic cost function,

$$\Gamma=\sum_v\left\{\Phi_{0,v}-\sum_{e\in E_v}w_e\Phi_e\right\}^2+\sum_e\left(\alpha_1\frac{f_e^2}{K_e}+\alpha_0K_e^{\frac{1}{2}}\right). \tag{25}$$

To reduce complexity we set $w_e=1$, granting each vessel the same supply effectiveness. It should be noted that in this particular model framework, each absorbing volume only needs to be in touch with at least one supplying vessel to ensure supply, in principal. In order to ensure the same amount of initial vessels per service volume and vice versa, we impose periodic boundaries on the system. For the moment, we define each independent, shortest cycle in the graph as a service volume. Given a hexagonal lattice this means each volume is to be affiliated with six edges. In any system with periodic boundaries we impose a single source with solute influx on a random position and a single sink with absorbing boundary on one of the topologically most distant sites, see Fig. 2(b). We set the volume demands $\Phi_{0,v}$ such that the network's demanded filtration rate would correspond to

$$\sigma_0=\log_{10}\left[\frac{\sum_v\Phi_{0,v}}{\sum_{v,J_v>0}J_v}\right]. \tag{26}$$

For the presented simulations, we initialize $\Phi_{0,v}$ homogeneously across the network, as we do for β^*. As described in the previous section, we find the system's stationary states and analyze those for their nullity ϱ and actual filtration rate σ, as defined in the previous Sec. II D. Note that nonzero nullity, for periodic boundaries, may correspond to the existence of topological generators (cycles created by walking through the periodic boundaries) [48].

Once again we focus on three significant (σ_0,β^*) variations as depicted in Figs. 5 and 6. Surprisingly we find that the nature of topological transitions and filtration regimes is mostly preserved with regard to link-wise supply: As before, in the case of $\sigma_0=0$ and $\beta^*=10^{-3}$, we observe the formation of dilated bulk vessels with collapsing peripheries, dangling branches as well as shunting for high demand and low absorption rates, see Figs. 5(a) and 6(a). The emergence of flow bottlenecks seems to be a recurring motif due to the choice of Neumann boundaries. Note that the resulting network redundancy becomes more sensitive to the plexus random radii initialization as well as the fact that full plexus

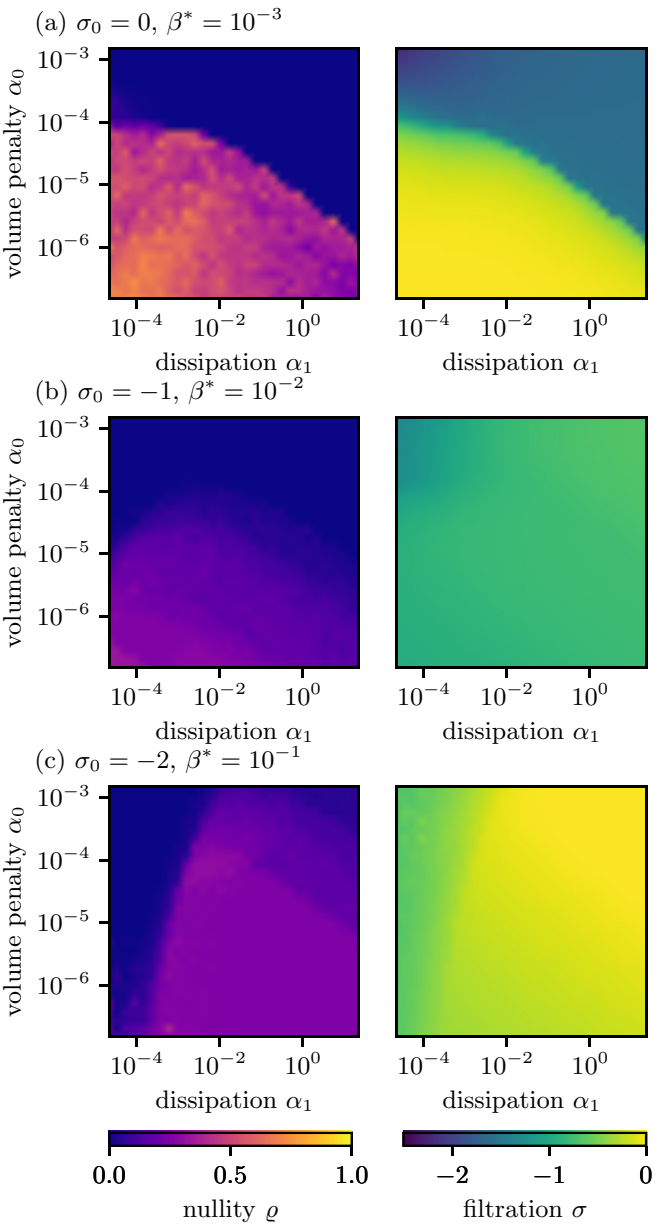

FIG. 5. Stationary states for the volume-wise demand-supply problem (25). Color-coded state diagrams indicate network nullity ϱ (left column) and accumulated filtration σ (right column) for selected (σ_0,β^*).

recovery becomes unlikely. Further we find the topological transition once again to correlate with the breakdown of filtration. Turning toward the regime featuring reduced demand paired with increased absorption capability, $\sigma_0=-1$ and $\beta^*=10^{-2}$, one again observes the emergence of reentrant behavior, see Figs. 5(b) and 6(b). Nevertheless, the filtration demand is met in good agreement with the target unless increased α_0 is considered. Note that the redundancy during this reentry is mostly generated due to vessel paths enclosing multiple merged tiles. Finally, we consider the case of low demand and high absorption rates, see Figs. 5(c) and 6(c). We notice the emergence of nullity re-entrance and considerable mismatch of the resulting filtration with its initial demand in

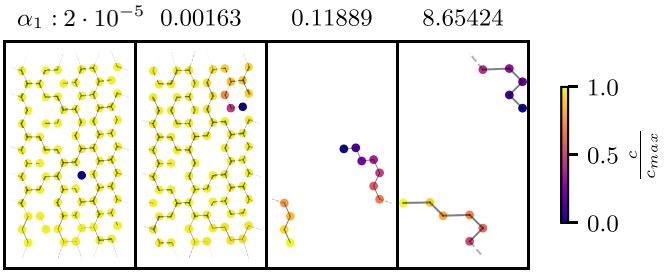

(a) $\sigma_0 = 0$, $\beta^* = 10^{-3}$, $\alpha_0 = 2.4 \cdot 10^{-5}$

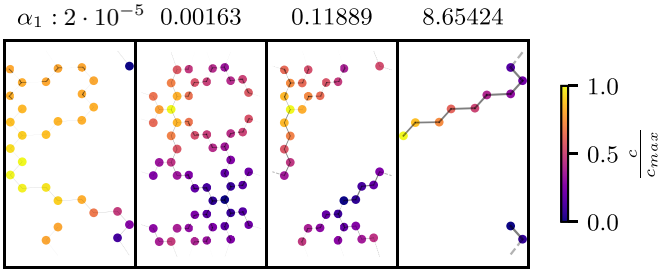

(b) $\sigma_0 = -1$, $\beta^* = 10^{-2}$, $\alpha_0 = 2.4 \cdot 10^{-5}$

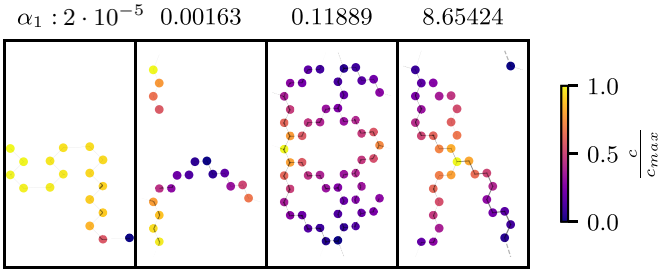

(c) $\sigma_0 = -2$, $\beta^* = 10^{-1}$, $\alpha_0 = 10^{-3}$

FIG. 6. Stationary network formations for the volume-wise demand-supply problem: Depicted are formations for selected demands σ_0, absorption rates β^*, volume penalties α_0, and dissipation feedbacks α_1 after minimizing (25). All systems were initialized with a single sink-source dipole and periodic boundaries. The nodal concentrations are color coded and link thickness is indicating edge radii.

case of the unfavorable parameter combinations $\sigma_0 = -2$ and $\beta^* = 10^{-1}$.

IV. DISCUSSION

In this study we have shown that demand-supply driven remodeling can be severely perturbed by wall-shear stress driven adaptation and vice versa. Given the particular demand-supply mismatches $S(\mathbf{\Phi}, \mathbf{\Phi}_0)$, e.g., weakly absorbing vessels paired with high demand service volumes, we have shown the existence of a nullity transition in combination with the formation of frustrated structures, such as bottlenecks and dangling branches.

Further we observed the emergence of nullity re-entrant behavior for strongly absorbing, low demand service volumes, and find its existence for both link- or volume based mismatch scenarios $S(\mathbf{\Phi}, \mathbf{\Phi}_0)$. Neither periodic boundaries nor the restructuring of injection points seem to alter the qualitative behavior of the adaptation process, i.e., the occurrence of topological transitions. Generally we find the establishment of homogeneous uptake patterns in the network for negligible dissipation feedback α_1, see Appendix C, in accordance to studies on purely metabolite optimized systems [3]. Overall we find wall-shear stress based adaptation and metabolite uptake optimization to be competing mechanisms leading to hydrodynamically unfavorable vessel formations, when absorption rates β^* are poorly adjusted with regard to the supply-demand mismatch $S(\mathbf{\Phi}, \mathbf{\Phi}_0)$. It seems unlikely although that real biological systems operate in this regime unless forced to do so, e.g., due to pathological ramifications. One may argue that these phenomena arise due to the shortcomings of the model framework, as we consider (incompressible) Hagen-Poiseuille flow with Neumann boundaries. Due to these model characteristics arbitrarily large pressure gradients and shear stresses may be present without leading to catastrophic failure of the actual network. At the very least it indicates a limit of the applicability to Kirchhoff network based adaptation schemes.

As was demonstrated in [3,4], optimizing a flow network for homogeneous solute uptake alone will not spark topological transitions or pruning events whatsoever. Yet, we do not find the metabolite uptake mechanism to ensure stabilization of space-filling, robust vessel systems in case of increased volume penalties. On the contrary, we found that without any dissipation feedback considered, large network sections can collapse and fracture. This seems to hold true for either demand-supply scenario, as even in the case of volume supply we do not find the uptake mechanism to necessarily stabilize the minimal amount of vessels in contact with each service volume. Future studies should therefore consider diverging penalties in case of degeneration of all affiliated vessels to avoid catastrophic outcomes, similar to previous heuristic models [32].

Further, assuming homogeneous demand and absorption rates, we find a transition between metabolic zonation scenarios, as previously discussed by Meigel *et al.* [3], see Appendix C. Hence, in comparison to real capillary systems, we find our model to account for homogeneously supplied structures, e.g., as found in zebrafish vasculature, where flow uniformity was considered as a crucial factor in development [5,24]. On the other hand, it appears that wall-shear stress driven adaptation worsens the demand-supply mismatch as the bulk of absorbing vessels is pruned down to a few conducting channels corresponding to a set of linear channel solutions. The emergence of dangling branches and bottlenecks seems more relevant as these correspond to formations found in pathological vessel development, e.g., in cases of tumor driven sprouting or stenosis.

We nevertheless come to the conclusion that the adjustment of flow landscapes via radial adaptation alone poses very limited potential to ensure metabolite uptake and hydrodynamic efficiency simultaneously. That is, if the demand-supply mismatch is unfavorable with regard to σ_0 and β^*. Which gives rise to a set of potential new questions:

How effective may tissue elements regulate β^* as to adjust local uptake given a flux, i.e., by modifying membrane porosity, density of transporters, internal enzyme levels for clearance or storage capabilities? How effectively are tissues able to regulate their responses and readjust volume penalties and dissipation feedback for quickly altering metabolite demands, e.g., in case of organism growth or tumor angiogenesis? Are corresponding elements of σ_0, β^* regulated by cells in order to prevent frustrated formations? Is the appearance of unfavorable demand-supply scenarios symptom of a real pathological state?

We think that the current models of antagonistic adaptation mechanisms, flux or demand-supply based, are in need of further improvement. In terms of cost-optimization models we propose a leap-frog-style adaptation where a solute uptake optimization follows a conventional dissipation-volume optimizing system. Considering the conventional stress driven adaptation schemes with cost rescaling [45] and stochastic flow patterns [22,49] one may still generate topological complex, space-filling structures, or reach those by different dynamic environments [21,50]. Yet, instead of readjusting radii directly given the tissue's metabolic demands in terms of oxygen, glucose etc., we suggest that once a space-filling perfusion is reached, a secondary optimization takes place adjusting β^*. Unlike changing the flow pattern, and therefore clashing with shear stress adaptation, regulation of Φ_e would take place locally at the membrane-tissue interface. We think this ansatz to be promising in particular in the case of complex embedded networks with metabolic zonation, such as found in the liver lobule [51], where elaborate membrane dynamics and clearance mechanisms ensure the transport of metabolites between multiple flow networks and mediating cell layers [52].

It has further been argued that the metabolic dynamics in such a system would be dependent on the concentration gradients of various metabolites [53], which would correspond to sophisticated $\beta^*(c)$ in our current framework. Such elaborate attempts would likely have to take into account the clearance capacities and kinetics of the surrounding tissues. Vessel size dependencies might be considered as well as for absorption rates, e.g., $\beta^*(r) = \beta_0^* + \beta_1^* r + \beta_2^* r^2 + ...$, in order to account for alteration of the membrane characteristics of growing or shrinking vessels. Eventually we envision this class of models to create a better understanding of the formation and maintenance of these complex intertwined systems, ultimately illuminating the relevant transport mechanism in these organs.

Note added. We became aware of related work by Gounaris *et al.* [54].

ACKNOWLEDGMENTS

F.K. gratefully acknowledges support from the German Federal Ministry of Education and Research (BMBF), Grant No. 031L0044 (SYSBIO II). Our thanks go to Felix Meigel, Karen Alim, Benjamin Friedrich, Marino Zerial, and Yannis Kalaidzidis for their insightful feedback during the development and implementation of the model, as well as for their constructive feedback regarding the manuscript. Further thanks go out to the members of the Modes Lab, Zechner Lab, Huch Lab, Honigmann Lab and Grapin-Botton Lab of the CSBD and MPI-CBG.

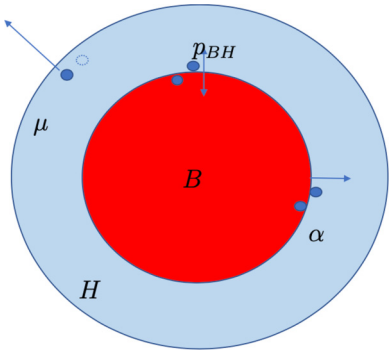

FIG. 7. Cross-section representation of a metabolite perfused vessel B, embedded in a tissue H, with consideration of diffusion p_{BH}, active transport α and clearance μ, taken from [57].

APPENDIX A: METABOLITE TRANSPORT IN CHANNELS AND ARBITRARY KIRCHHOFF NETWORKS

Our model can be seen as the limit case of a class of more elaborate transport models used for organ level metabolite processing [55,56], which we will discuss in the following on the basis of [57]. Consider the blood vessel (B) evenly surrounded by a relevant section of tissue (e.g., hepatocytes, H), see Fig. 7. The solute is distributed over the length of the vessel such that we only care for its axial dependency. The actual uptake process is here split into three main components: diffusion across the membrane with effective permeability p_{BH}, active transport α by membrane proteins and tissue clearance μ. With clearance we refer to metabolic processing of the particular chemical species as well as transport, i.e., diffusion or secretion, into different parts of the organ. Considering these processes, one could formulate the concentration dynamics, resulting continuity equations for the tissue c_H and the blood c_B as

$$\partial_t c_H(z) = p_{BH}[c_B(z) - c_H(z)] + \alpha c_B(z) - \mu c_H(z), \tag{A1}$$

$$\partial_t c_B(z) = D\partial_{zz} c_B(z) - \bar{v}\partial_z c_B(z) - p_{BH}[c_B(z) - c_H(z)] - \alpha c_B(z). \tag{A2}$$

While the solute clearance is only linearly dependent in this representation, one should be reminded that metabolic processing often is enzyme dependent. On the same note one can assume that transporter proteins in the membrane have an upper capacity. Hence first approximations capturing this behavior are usually Michaelis–Menten like kinetics of the form

$$\alpha \to \frac{\alpha_1}{\alpha_0 + c_B} = \alpha(c_B), \tag{A3}$$

$$\mu \to \frac{\mu_1}{\mu_0 + c_H} = \mu(c_H). \tag{A4}$$

Hence active transport and clearance is pending between two limit cases of unsaturated linear behavior and a constant capacity limit. We focused in this study on the special case of unsaturated kinetics with $\alpha \to \alpha_1 = const$ and $\mu \to \mu_1 = const$.

Formulating the ODE systems for their steady states with that in mind we get

$$\partial_t c_H(z) = 0 \Rightarrow c_H(z) = c_B(z)\frac{p_{BH}+\alpha}{p_{BH}+\mu}, \tag{A5}$$

$$\partial_t c_B(z) = 0 \Rightarrow 0 = D\partial_{zz}c_B(z) - u\partial_z c_B(z) - \mu\frac{p_{BH}+\alpha}{p_{BH}+\mu}c_B(z). \tag{A6}$$

We may rewrite this in the form of the transport equations we were discussing all along by setting

$$\partial_{zz^*}c_B(z) = \mathrm{Pe}\partial_{z^*}c_B(z) + \bar{\beta}^* c_B(z) \tag{A7}$$

$$\text{with } \bar{\beta}^* = \mu\left(\frac{p_{BH}+\alpha}{p_{BH}+\mu}\right)\frac{L^2}{D}. \tag{A8}$$

Which is the model we actually followed up on here. Now, different behavior such as metabolite backflow and tissue saturation could also be captured by using the "Michaelis-Menten like" coefficients approach, but is currently beyond the scope of this study. The rest of this section is dedicated to a detailed derivation of the equation systems and solutions relevant to Sec. II B. Recall that the continuity equation in nondimensional form is

$$\bar{c}(z^*) = X_0 \mathrm{e}^{\lambda_0 z^*} + X_1 \mathrm{e}^{\lambda_0 z^*}, \tag{A9}$$

$$\text{with } \lambda_{0/1} = \tfrac{1}{2}(\mathrm{Pe} \pm \sqrt{\mathrm{Pe}^2 + \beta^*}), \tag{A10}$$

with channel boundaries $\bar{c}(z=0) = \bar{c}_0$, $\bar{c}(z=L) = \bar{c}_L$ and $X_0 = \frac{\bar{c}_L - \bar{c}_0 \mathrm{e}^{\lambda_1}}{\mathrm{e}^{\lambda_0} - \mathrm{e}^{\lambda_1}}$ and $X_1 = \frac{\bar{c}_0 \mathrm{e}^{\lambda_0} - \bar{c}_L}{\mathrm{e}^{\lambda_0} - \mathrm{e}^{\lambda_1}}$. In order to calculate the solute flux and the corresponding equation system for a complex network one writes (using $x_e = \sqrt{\mathrm{Pe}_e^2 + \beta_e^*}$)

$$I_k(z) = A_k[\bar{u}_k \bar{c}_k(z) - D\partial_z \bar{c}_k(z)] \tag{A11}$$

$$= \frac{A_k D}{L}[\mathrm{Pe}_k \bar{c}_k(z) - \partial_{z^*}\bar{c}_k(z)]$$

$$\Rightarrow I_k(0) = I_{\alpha(k)} \tag{A12}$$

$$= \frac{A_k D}{2L}\left\{\bar{c}_{\alpha(k)}\left[\mathrm{Pe}_k + x_k \coth\left(\frac{x_k}{2}\right)\right] - \bar{c}_{\omega(k)}\frac{x_k \mathrm{e}^{-\frac{\mathrm{Pe}_k}{2}}}{\sinh\left(\frac{x_k}{2}\right)}\right\}$$

$$\Rightarrow I_k(L) = I_{\omega(k)}$$

$$= \frac{A_k D}{2L}\left\{\bar{c}_{\omega(k)}\left[\mathrm{Pe}_k - x_k \coth\left(\frac{x_k}{2}\right)\right] + \bar{c}_{\alpha(k)}\frac{x_k \mathrm{e}^{\frac{\mathrm{Pe}_k}{2}}}{\sinh\left(\frac{x_k}{2}\right)}\right\}. \tag{A13}$$

Now we utilize the boundary conditions for solute flux on every node, using $\frac{A_k D}{L} = q_k$, so that we may write for in- and outflux of solute of a vertex,

$$J_i = \sum_k B_{ik} I_k = \sum_{k\in\mathrm{out}(i)} I_{\alpha(k)} - \sum_{k\in\mathrm{in}(i)} I_{\omega(k)}$$

$$= \sum_k q_k\left[B_{ik}\mathrm{Pe}_k + |B_{ik}| x_k \coth\left(\frac{x_k}{2}\right)\right]\bar{c}_i$$

$$- \sum_{k\in\mathrm{out}(i)} q_k \frac{x_k \mathrm{e}^{-\frac{\mathrm{Pe}_k}{2}}}{2\sinh\left(\frac{x_k}{2}\right)}\bar{c}_{\omega(k)}$$

$$- \sum_{k\in\mathrm{in}(i)} q_k \frac{x_k \mathrm{e}^{\frac{\mathrm{Pe}_k}{2}}}{2\sinh\left(\frac{x_k}{2}\right)}\bar{c}_{\alpha(k).} \tag{A14}$$

We rewrite this equation system according to [44] in vectorial form

$$\boldsymbol{M}\cdot\boldsymbol{c} = \boldsymbol{J}, \tag{A15}$$

which also allows us to efficiently solve for $\boldsymbol{c}$ for any given $\boldsymbol{J}$,

$$M_{ij} = \sum_k \frac{q_k}{2}\left[B_{ik}\mathrm{Pe}_k + |B_{ik}| x_k \coth\left(\frac{x_k}{2}\right)\right]\delta_{ij}$$

$$- \sum_{k\in\mathrm{out}(i)} q_k \frac{x_k \mathrm{e}^{-\frac{\mathrm{Pe}_k}{2}}}{2\sinh\left(\frac{x_k}{2}\right)}\delta_{\omega(k),j}$$

$$- \sum_{k\in\mathrm{in}(i)} q_k \frac{x_k \mathrm{e}^{\frac{\mathrm{Pe}_k}{2}}}{2\sinh\left(\frac{x_k}{2}\right)}\delta_{\alpha(k),j}. \tag{A16}$$

As we generally utilize mixed boundary conditions with $c_n = 0$ on the outflux periphery and $J_n > 0$ on the influx periphery of the network we can calculate the complementary missing values and subsequently calculate the linkwise metabolite absorption,

$$\Phi = \sum_i J_i \tag{A17}$$

$$= \sum_k \frac{q_k}{2}\left\{\bar{c}_{\alpha(k)}\left[x_k \coth\left(\frac{x_k}{2}\right) - \frac{x_k \mathrm{e}^{\frac{\mathrm{Pe}_k}{2}}}{\sinh\left(\frac{x_k}{2}\right)} + \mathrm{Pe}_k\right] + \bar{c}_{\omega(k)}\left[x_k \coth\left(\frac{x_k}{2}\right) - \frac{x_k \mathrm{e}^{-\frac{\mathrm{Pe}_k}{2}}}{\sinh\left(\frac{x_k}{2}\right)} - \mathrm{Pe}_k\right]\right\}$$

$$\Rightarrow \Phi_k = \frac{q_k}{2}\left\{\bar{c}_{\alpha(k)}\left[x_k \coth\left(\frac{x_k}{2}\right) - \frac{x_k \mathrm{e}^{\frac{\mathrm{Pe}_k}{2}}}{\sinh\left(\frac{x_k}{2}\right)} + \mathrm{Pe}_k\right] + \bar{c}_{\omega(k)}\left[x_k \coth\left(\frac{x_k}{2}\right) - \frac{x_k \mathrm{e}^{-\frac{\mathrm{Pe}_k}{2}}}{\sinh\left(\frac{x_k}{2}\right)} - \mathrm{Pe}_k\right]\right\}. \tag{A18}$$

In Fig. 8 we display an example solution for a single channel with absorbing boundary. One finds the concentration profile in general to become linear in the case of small Peclet numbers, corresponding to the maximal possible decline in solute flux, see Fig. 8(a). Further to get a quantitative and qualitative perspective on the metabolite uptake in this system one may consider the effective uptake, see Fig. 8(b). As depicted one finds the uptake to vary drastically with the Peclet numbers as well as the effective absorption rate. Note that increased Peclet numbers generally correspond to a decreased uptake while entering the diffusive regime for $Pe \to 0$ displays clear saturation behavior in dependence of β^*.

APPENDIX B: DEMAND-SUPPLY BASED ADAPTATION ALGORITHM

We formulate a dynamical system, which describes the adaptation of a vessel network in order to minimize the metabolic cost function Γ,

$$\Gamma = S(\boldsymbol{\Phi}, \boldsymbol{\Phi}_0) + \sum_e \left(\alpha_1 \frac{f_e^2}{K_e} + \alpha_0 K_e^\gamma\right). \tag{B1}$$

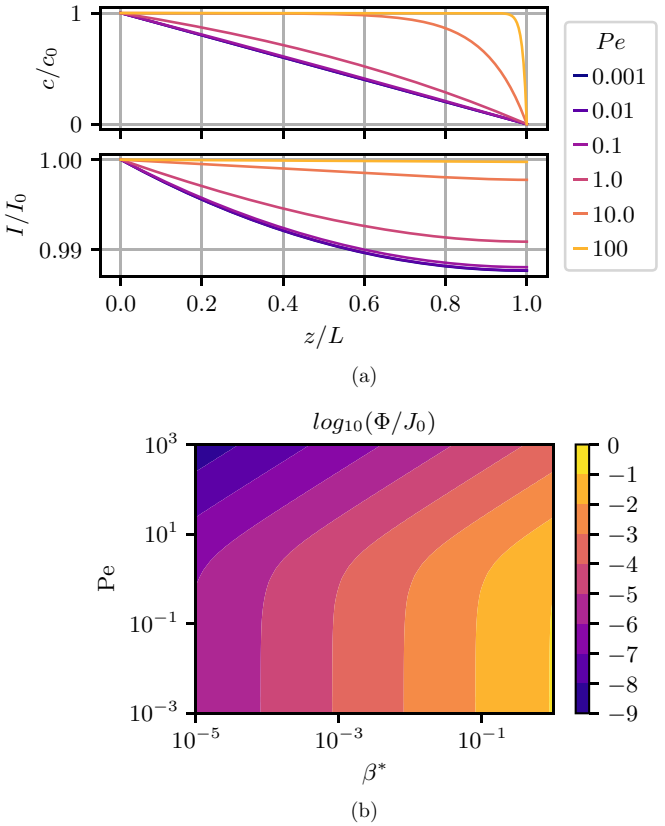

FIG. 8. Single channel solutions with absorbing boundary. (a) Concentration and solute flux profiles for $\beta^* = 10^{-2}$. (b) Effective metabolite uptake.

Following the gradient-descent approach in order to reach Lyapunov stable states we formulate the equations of motions as

$$\partial_t r_j = -\chi\, \partial_{r_j} \Gamma$$
$$\Rightarrow \frac{d}{dt}\Gamma = \nabla \Gamma^T \cdot \partial_t \boldsymbol{r} \leqslant 0, \forall \chi \geqslant 0. \tag{B2}$$

Subsequently this leads to

$$\partial_t r_j = -\chi\, \partial_{r_j} \Gamma \tag{B3}$$
$$= -\chi \sum_k \partial_{\Phi_k} S(\boldsymbol{\Phi}, \boldsymbol{\Phi}_0) \partial_{r_j} \Phi_k + \partial_{r_j} \sum_e \left(\alpha_1 \frac{f_e^2}{K_e} + \alpha_0 K_e^\gamma \right). \tag{B4}$$

The last term in Eq. (B5), concerning the derivatives of the dissipation-volume costs, has been discussed in previous studies, e.g., [50]. Subsequently we proceed with the metabolic uptake problem. First, we rewrite the uptake term Φ_k for an arbitrary link k as

$$\Phi_k = \frac{q_k}{2}(\bar{c}_{\alpha(k)} G_k + \bar{c}_{\omega(k)} H_k) \tag{B5}$$

with subfunctions defined as

$$G_k = \left[x_k \coth\left(\frac{x_k}{2}\right) - \frac{x_k e^{\frac{\mathrm{Pe}_k}{2}}}{\sinh\left(\frac{x_k}{2}\right)} + \mathrm{Pe}_k \right], \tag{B6}$$

$$H_k = \left[x_k \coth\left(\frac{x_k}{2}\right) - \frac{x_k e^{-\frac{\mathrm{Pe}_k}{2}}}{\sinh\left(\frac{x_k}{2}\right)} - \mathrm{Pe}_k \right], \tag{B7}$$

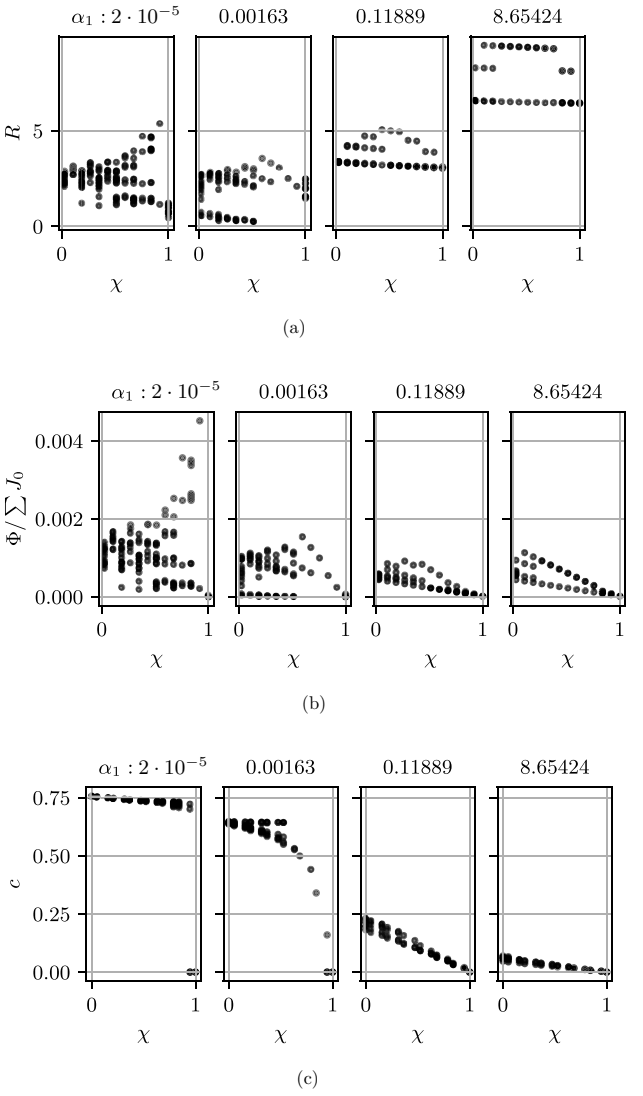

FIG. 9. Radii, effective uptake and concentration profiles from source ($\chi = 0$) to sink ($\chi = 1$) for high demand and low absorption rates $\sigma_0 = 10^0$, $\beta^* = 10^{-3}$, $\alpha_0 = 4.5 \times 10^{-5}$, referring to the link-wise demand-supply scenario in hexagonal grids.

and partial derivatives (using notation $\partial_{r_j}[\cdot] = \partial_j[\cdot]$) calculated to be

$$\partial_j \Phi_k = \partial_j \frac{q_k}{2}(\bar{c}_{\alpha(k)} G_k + \bar{c}_{\omega(k)} H_k)$$
$$+ \frac{q_k}{2}(\partial_j \bar{c}_{\alpha(k)} G_k + \partial_j \bar{c}_{\omega(k)} H_k)$$
$$+ \frac{q_k}{2}(\bar{c}_{\alpha(k)} \partial_j G_k + \bar{c}_{\omega(k)} \partial_j H_k), \tag{B8}$$

$$\partial_j q_k = 2\pi R_k \delta_{jk}, \tag{B9}$$

$$\partial_j c_i = \partial_j (\boldsymbol{e}_i^T \cdot \boldsymbol{c}) = \boldsymbol{e}_i^T \cdot \partial_j (\boldsymbol{M}^\dagger \boldsymbol{J}) \tag{B10}$$

$$= -\boldsymbol{e}_i^T \cdot (\boldsymbol{M}^\dagger \partial_j \boldsymbol{M} \boldsymbol{M}^\dagger \boldsymbol{J}) \tag{B11}$$

$$= -\boldsymbol{e}_i^T \cdot (\boldsymbol{M}^\dagger \partial_j \boldsymbol{M} \boldsymbol{c}). \tag{B12}$$

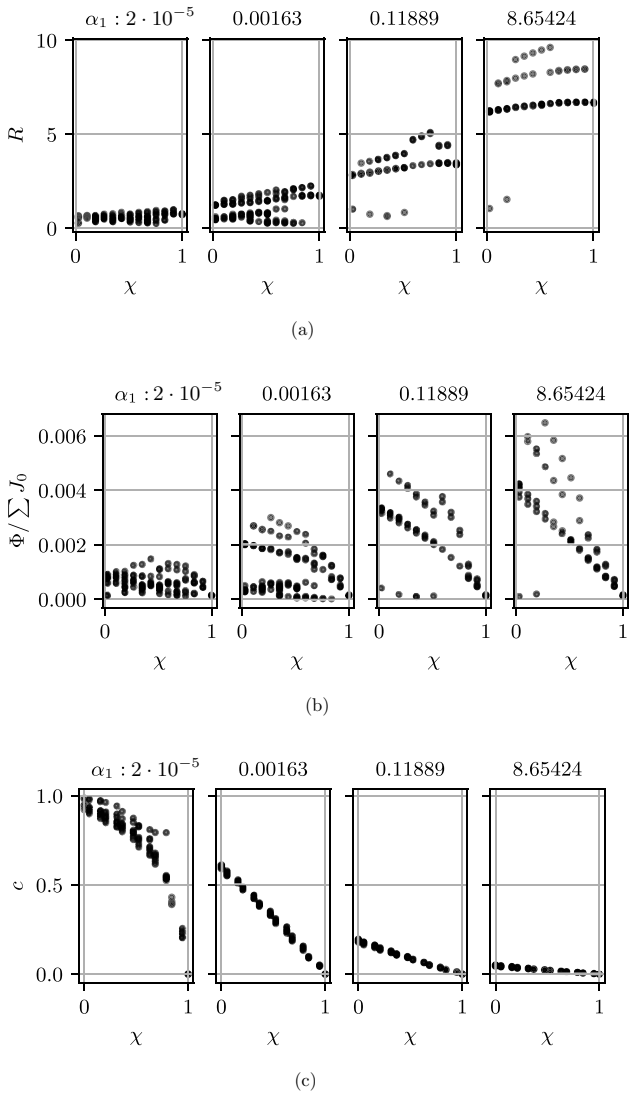

FIG. 10. Radii, effective uptake and concentration profiles from source ($\chi = 0$) to sink ($\chi = 1$) for mediocre demand and mediocre absorption rates $\sigma_0 = 10^{-1}$, $\beta^* = 10^{-2}$, $\alpha_0 = 4.5 \times 10^{-5}$, referring to the linkwise demand-supply scenario in hexagonal grids.

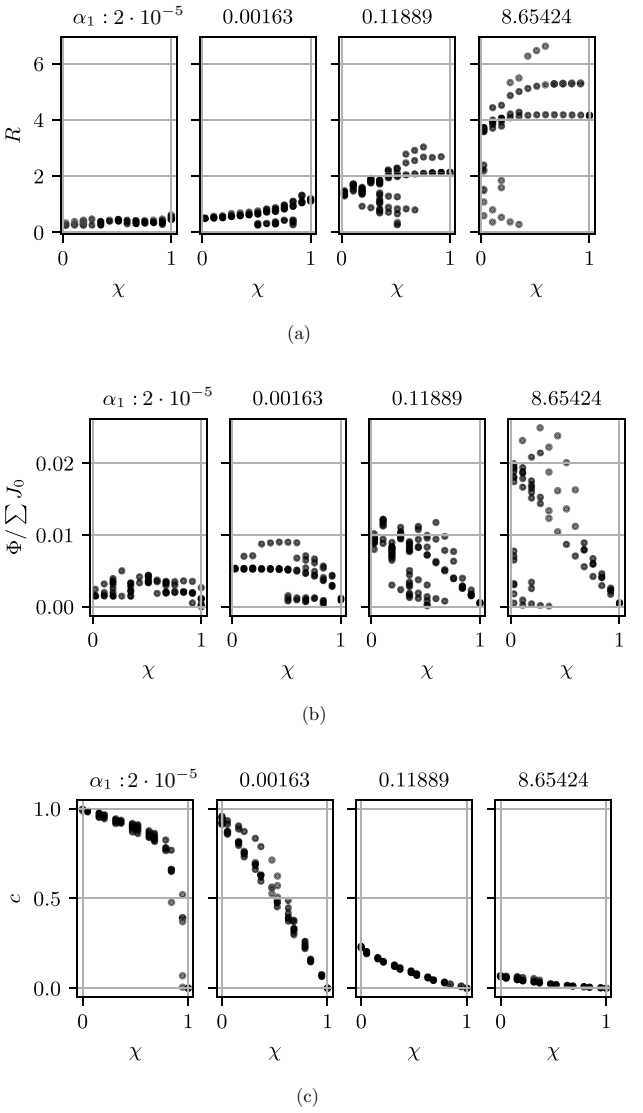

FIG. 11. Radii, effective uptake and concentration profiles from source ($\chi = 0$) to sink ($\chi = 1$) for low demand and high absorption rates $\sigma_0 = 10^{-2}$, $\beta^* = 10^{-1}$, $\alpha_0 = 8 \times 10^{-8}$, referring to the linkwise demand-supply scenario in hexagonal grids.

Subsequently we can calculate the derivatives of $\boldsymbol{M}$ and the subcomponents as

$$\partial_j M_{ij} = \sum_k \partial_j \frac{q_k}{2}\left[B_{ik}\mathrm{Pe}_k + |B_{ik}|x_k \coth\left(\frac{x_k}{2}\right)\right]\delta_{ij} + \sum_k \frac{q_k}{2}B_{ik}\partial_j \mathrm{Pe}_k \delta_{ij} + \sum_k \frac{q_k}{2}|B_{ik}|\left\{\frac{\coth\left(\frac{x_k}{2}\right)}{x_k} - \left[\frac{\coth\left(\frac{x_k}{2}\right)}{\cosh\left(\frac{x_k}{2}\right)}\right]^2\right\}\partial_j \mathrm{Pe}_k \delta_{ij}$$

$$- \sum_{k\in\mathrm{out}(i)} \partial_j \frac{q_k}{2}\frac{x_k \mathrm{e}^{-\frac{\mathrm{Pe}_k}{2}}}{\sinh\left(\frac{x_k}{2}\right)}\delta_{\omega(k),j} + \sum_{k\in\mathrm{out}(i)} \frac{q_k}{2}\frac{\mathrm{e}^{-\frac{\mathrm{Pe}_k}{2}}}{\sinh\left(\frac{x_k}{2}\right)}\left[\frac{\mathrm{Pe}_k}{x_k} - \frac{x_k}{2} - \frac{\mathrm{Pe}_k}{2}\coth\left(\frac{x_k}{2}\right)\right]\partial_j \mathrm{Pe}_k \delta_{\omega(k),j}$$

$$- \sum_{k\in\mathrm{in}(i)} \partial_j \frac{q_k}{2}\frac{x_k \mathrm{e}^{-\frac{\mathrm{Pe}_k}{2}}}{\sinh\left(\frac{x_k}{2}\right)}\delta_{\alpha(k),j} + \sum_{k\in\mathrm{in}(i)} \frac{q_k}{2}\frac{\mathrm{e}^{-\frac{\mathrm{Pe}_k}{2}}}{\sinh\left(\frac{x_k}{2}\right)}\left[\frac{\mathrm{Pe}_k}{x_k} + \frac{x_k}{2} - \frac{\mathrm{Pe}_k}{2}\coth\left(\frac{x_k}{2}\right)\right]\partial_j \mathrm{Pe}_k \delta_{\alpha(k),j}, \tag{B13}$$

$$\partial_j G_k = \frac{\partial_j \mathrm{Pe}_k}{\sinh\left(\frac{x_k}{2}\right)}\left\{\frac{\mathrm{Pe}_k}{x_k}\left[\cosh\left(\frac{x_k}{2}\right) - \mathrm{e}^{\frac{\mathrm{Pe}_k}{2}}\right] + \sinh\left(\frac{x_k}{2}\right) - \frac{\mathrm{Pe}_k}{2\sinh\left(\frac{x_k}{2}\right)} + \mathrm{e}^{\frac{\mathrm{Pe}_k}{2}}\left[\frac{\mathrm{Pe}_k}{2}\coth\left(\frac{x_k}{2}\right) - \frac{x_k}{2}\right]\right\}, \tag{B14}$$

$$\partial_j H_k = \frac{\partial_j \mathrm{Pe}_k}{\sinh\left(\frac{x_k}{2}\right)}\left\{\frac{\mathrm{Pe}_k}{x_k}\left[\cosh\left(\frac{x_k}{2}\right) - \mathrm{e}^{-\frac{\mathrm{Pe}_k}{2}}\right] - \sinh\left(\frac{x_k}{2}\right) - \frac{\mathrm{Pe}_k}{2\sinh\left(\frac{x_k}{2}\right)} + \mathrm{e}^{-\frac{\mathrm{Pe}_k}{2}}\left[\frac{\mathrm{Pe}_k}{2}\coth\left(\frac{x_k}{2}\right) + \frac{x_k}{2}\right]\right\}. \tag{B15}$$

Finally we calculate the derivatives of the local Peclet numbers as

$$\partial_j \mathrm{Pe}_k = \frac{L_k}{D}\partial_j \bar{u}_k \tag{B16}$$

$$= \frac{1}{8\eta L_k}\left(2\delta_{jk} R_k \Delta p_k + R_k^2 \partial_j \Delta p_k\right)$$

$$\text{with } \partial_j \bar{u}_k = \partial_j\left(\frac{R_k^2 \Delta p_k}{8\eta L_k}\right). \tag{B17}$$

We compute the pressure derivatives from the Kirchhoff solutions as

$$\partial_j \Delta p_k = \partial_j\left[\boldsymbol{e}_k^T \boldsymbol{B}^T (\boldsymbol{B}\boldsymbol{C}\boldsymbol{B}^T)^\dagger \boldsymbol{s}\right] \tag{B18}$$

$$= -\boldsymbol{e}_k^T \boldsymbol{B}^T [\boldsymbol{B}\boldsymbol{C}\boldsymbol{B}^T]^\dagger \boldsymbol{B}\partial_j \boldsymbol{C}\Delta \boldsymbol{p} \tag{B19}$$

$$= -\boldsymbol{e}_k^T \boldsymbol{B}^T [\boldsymbol{B}\boldsymbol{C}\boldsymbol{B}^T]^\dagger \boldsymbol{B}\left[\frac{4C_j}{R_j}(\boldsymbol{e}_j \otimes \boldsymbol{e}_j)\right]\Delta \boldsymbol{p} \tag{B20}$$

$$= -\frac{4C_j \Delta p_j}{R_j}(\boldsymbol{B}^T [\boldsymbol{B}\boldsymbol{C}\boldsymbol{B}^T]^\dagger \boldsymbol{B})_{jk}, \tag{B21}$$

which closes the system derivatives for $\partial_t r_i$ and allows us to evaluate the flow landscape as well as the occurring gradients accordingly.

APPENDIX C: CONCENTRATIONS, UPTAKE, AND RADIAL PATTERNS IN OPTIMIZED FLOW NETWORKS

In this section we present additional material on the systematic parameter scan of linkwise demand-supply adaptation, as described in the results Sec. II. The diagrams depict the nodal concentrations, uptake effectiveness, and radial distributions for the selected σ_0, β^*, α_0, and α_1 variations depicted in Figs. 3 and 4, i.e. high demand and low absorption rates (Fig. 9), mediocre demand and mediocre absorption rates (Fig. 10), and low demand and high absorption rates (Fig. 11). The χ notation depicts the relative distance of the respective vertex, or link center of the nearest source node, i.e., $\chi = 0$ corresponds to a source node while $\chi = 1$ describes sink-sided positions.

[1] C. D. Murray, The physiological principle of minimum work: I. the vascular system and the cost of blood volume., Proc. Natl. Acad. Sci. USA **12**, 207 (1926).

[2] F. J. Meigel, P. Cha, M. P. Brenner, and K. Alim, Robust Increase in Supply by Vessel Dilation in Globally Coupled Microvasculature, Phys. Rev. Lett. **123**, 228103 (2019).

[3] F. J. Meigel and K. Alim, Flow rate of transport network controls uniform metabolite supply to tissue, J. R. Soc. Interface **15**, 20180075 (2018).

[4] T. Gavrilchenko and E. Katifori, Distribution Networks Achieve Uniform Perfusion through Geometric Self-Organization, Phys. Rev. Lett. **127**, 078101 (2021).

[5] S.-S. Chang and M. Roper, Microvscular networks with uniform flow., J. Theor. Biol. **462**, 48 (2019).

[6] P. F. Davies, Flow-mediated endothelial mechanotransduction, Physiol. Rev. **75**, 519 (1995).

[7] A. R. Pries and T. W. Secomb, Modeling structural adaptation of microcirculation, Microcirculation **15**, 753 (2008).

[8] W. Risau, Mechanisms of angiogenesis, Nature (London) **386**, 671 (1997).

[9] K. Ljung, R. P. Bhalerao, and G. Sandberg, Sites and homeostatic control of auxin biosynthesis in *Arabidopsis* during vegetative growth, Plant J. **28**, 465 (2001).

[10] T.-H. Nguyen, A. Eichmann, F. Le Noble, and V. Fleury, Dynamics of vascular branching morphogenesis: The effect of blood and tissue flow, Phys. Rev. E **73**, 061907 (2006).

[11] A. R. Pries, T. W. Secomb, and P. Gaehtgens, Design principles of vascular beds, Circ. Res. **77**, 1017 (1995).

[12] A. Lenard, S. Daetwyler, C. Betz, E. Ellertsdottir, H.-G. Belting, J. Huisken, and M. Affolter, Endothelial cell self-fusion during vascular pruning, PLOS Biol. **13**, e1002126 (2015).

[13] S. B. Dahl-Jensen, S. Yennek, L. Flasse, H. L. Larsen, D. Sever, G. Karremore, I. Novak, K. Sneppen, and A. Grapin-Botton, Deconstructing the principles of ductal network formation in the pancreas, PLOS Biol. **16**, e2002842 (2018).

[14] A. Roth-Nebelsick, Evolution and function of leaf venation architecture: A review, Ann. Botany **87**, 553 (2001).

[15] A. Tero, R. Kobayashi, and T. Nakagaki, A mathematical model for adaptive transport network in path finding by true slime mold, J. Theor. Biol. **244**, 553 (2007).

[16] J. Karschau, A. Scholich, J. Wise, H. Morales-Navarrete, Y. Kalaidzidis, M. Zerial, and B. M. Friedrich, Resilience of three-dimensional sinusoidal networks in liver tissue, PLoS Comput. Biol. **16**, e1007965 (2020).

[17] C. G. Caro, T. J. Pedley, R. C. Schroter, W. A. Seed, and K. H. Parker, *The Mechanics of the Circulation*, 2nd ed. (Cambridge University Press, Cambridge, 2011).

[18] T. F. Sherman, On connecting large vessels to small. The meaning of Murray's law, J. Gen. Physiol. **78**, 431 (1981).

[19] A. Tero, S. Takagi, T. Saigusa, K. Ito, D. P. Bebber, M. D. Fricker, K. Yumiki, R. Kobayashi, and T. Nakagaki, Rules for biologically inspired adaptive network design, Science **327**, 439 (2010).

[20] J. Gräwer, C. D. Modes, M. O. Magnasco, and E. Katifori, Structural self-assembly and avalanchelike dynamics in locally adaptive networks, Phys. Rev. E **92**, 012801 (2015).

[21] H. Ronellenfitsch and E. Katifori, Global Optimization, Local Adaptation, and the Role of Growth in Distribution Networks, Phys. Rev. Lett. **117**, 138301 (2016).

[22] H. Ronellenfitsch and E. Katifori, Phenotypes of Vascular Flow Networks, Phys. Rev. Lett. **123**, 248101 (2019).

[23] D. Hu, D. Cai, and A. V. Rangan, Blood vessel adaptation with fluctuations in capillary flow distribution, PLoS ONE **7**, e45444 (2012).

[24] S.-S. Chang, S. Tu, K. I. Baek, A. Pietersen, Y.-H. Liu, V. M. Savage, S.-P. L. Hwang, T. K. Hsiai, and M. Roper, Optimal occlusion uniformly partitions red blood cells fluxes within a microvascular network, PLoS Comput. Biol. **13**, e1005892 (2017).

[25] R. Brandes, F. Lang, R. Schmidt, Robert F. Brandes, F. Lang, and R. F. Schmidt, *Lehrbuch*, 32nd ed. (Springer, Berlin, 2019).

[26] T. H. Adair, W. J. Gay, and J. P. Montani, Growth regulation of the vascular system: Evidence for a metabolic hypothesis, Am. J. Physiol. **259**, R393 (1990).

[27] A. R. Pries, A. J. M. Cornelissen, A. A. Sloot, M. Hinkeldey, M. R. Dreher, M. Höpfner, M. W. Dewhirst, and T. W. Secomb, Structural adaptation and heterogeneity of normal and tumor microvascular networks, PLoS Comput. Biol. **5**, e1000394 (2009).

[28] D. Ribatti and F. Pezzella, Overview on the different patterns of tumor vascularization, Cells **10**, 639 (2021).

[29] M. Welter and H. Rieger, Computer simulations of the tumor vasculature: Applications to interstitial fluid flow, drug delivery, and oxygen supply, in *Systems Biology of Tumor Microenvironment: Quantitative Modeling and Simulations*, edited by K. A. Rejniak (Springer International Publishing, Cham, 2016) pp. 31–72.

[30] B. Grigoryan, S. J. Paulsen, D. C. Corbett, D. W. Sazer, C. L. Fortin, A. J. Zaita, P. T. Greenfield, N. J. Calafat, J. P. Gounley, A. H. Ta *et al.*, Multivascular networks and functional intravascular topologies within biocompatible hydrogels, Science **364**, 458 (2019).

[31] X. Wang, Q. Sun, and J. Pei, Microfluidic-based 3d engineered microvascular networks and their applications in vascularized microtumor models, Micromachines **9**, 493 (2018).

[32] A. R. Pries, T. W. Secomb, and P. Gaehtgens, Structural adaptation and stability of microvascular networks: Theory and simulations, Am. J. Physiol. **275**, H349 (1998).

[33] T. W. Secomb, J. P. Alberding, R. Hsu, M. W. Dewhirst, and A. R. Pries, Angiogenesis: An adaptive dynamic biological patterning problem, PLoS Comput. Biol. **9**, e1002983 (2013).

[34] G. I. Taylor, Dispersion of soluble matter in solvent flowing slowly through a tube, Proc. R. Soc. London A **219**, 186 (1953).

[35] A. Krogh, The number and distribution of capillaries in muscles with calculations of the oxygen pressure head necessary for supplying the tissue., J. Physiol. (London) **52**, 409 (1919).

[36] K. Alim, G. Amselem, F. Peaudecerf, M. P. Brenner, and A. Pringle, Random network peristalsis in *Physarum polycephalum* organizes fluid flows across an individual, Proc. Natl. Acad. Sci. USA **110**, 13306 (2013).

[37] S. Marbach, K. Alim, N. Andrew, A. Pringle, and M. P. Brenner, Pruning to Increase Taylor Dispersion in *Physarum polycephalum* Networks, Phys. Rev. Lett. **117**, 178103 (2016).

[38] G. Birkhoff and J. B. Diaz, Non-linear network problems, Q. Appl. Math. **13**, 431 (1956).

[39] R. Penrose, A generalized inverse for matrices, in *Proceedings of the Cambridge Philosophical Society* (Cambridge University Press, Cambridge, 1955) pp. 406–413.

[40] C. A. Desoer and E. S. Kuh, *Basic Circuit Theory* (McGraw-Hill, New York, 1969).

[41] L. D. Landau and E. M. Lifshitz, *Fluid Mechanics*, 2nd ed., Course of Theoretical Physics (V.6) (Elsevier, Butterworth-Heinemann, Amsterdam, 2012).

[42] L. L. M. Heaton, E. Lopez, P. K. Maini, M. D. Fricker, and N. S. Jones, Advection, diffusion, and delivery over a network, Phys. Rev. E **86**, 021905 (2012).

[43] Created with biorender.com (2021).

[44] J. Koplik, S. Redner, and D. Wilkinson, Transport and dispersion in random networks with percolation disorder., Phys. Rev. A **37**, 2619 (1988).

[45] S. Bohn and M. O. Magnasco, Structure, Scaling, and Phase Transition in the Optimal Transport Network, Phys. Rev. Lett. **98**, 088702 (2007).

[46] D. Hu and D. Cai, Adaptation and Optimization of Biological Transport Networks, Phys. Rev. Lett. **111**, 138701 (2013).

[47] H. Whitney, Non-separable and planar graphs, Trans. Amer. Math. Soc. **34**, 339 (1932).

[48] C. D. Modes, M. O. Magnasco, and E. Katifori, Extracting Hidden Hierarchies in 3D Distribution Networks, Phys. Rev. X **6**, 031009 (2016).

[49] E. Katifori, G. J. Szollosi, and M. O. Magnasco, Damage and Fluctuations Induce Loops in Optimal Transport Networks, Phys. Rev. Lett. **104**, 048704 (2010).

[50] F. Kramer and C. D. Modes, How to pare a pair: Topology control and pruning in intertwined complex networks, Phys. Rev. Res. **2**, 043171 (2020).

[51] J. J. Gumucio, Functional and anatomic heterogeneity in the liver acinus: Impact on transport, Am. J. Physiol. **244**, G578 (1983).

[52] K. Si-Tayeb, F. P. Lemaigre, and S. A. Duncan, Organogenesis and development of the liver, Dev. Cell **18**, 175 (2010).

[53] N. Berndt, M. S. Horger, S. Bulik, and H.-G. Holzhütter, A multiscale modelling approach to assess the impact of metabolic zonation and microperfusion on the hepatic carbohydrate metabolism, PLoS Comput. Biol. **14**, e1006005 (2018).

[54] G. Gounaris, M. R. Garcia, and E. Katifori, Distribution efficiency and structure of complex networks, arXiv:2111.04657.

[55] M. S. Roberts and M. Rowland, A dispersion model of hepatic elimination: 1. Formulation of the model and bolus considerations, J. Pharmacokinet. Biopharm. **14**, 227 (1986).

[56] M. S. Roberts and M. Rowland, A dispersion model of hepatic elimination: 2. Steady-state considerations–influence of hepatic blood flow, binding within blood, and hepatocellular enzyme activity, J. Pharmacokinet. Biopharm. **14**, 261 (1986).

[57] F. Kramer, Characterization, analysis and modeling of complex flow networks in mammalian organs, Ph.D. thesis, Technische Universität Dresden, 2022.